The Astrophysical Journal, 932:76 (15pp), 2022 June 20 https://doi.org/10.3847/1538-4357/ac6e60

Long Dark Gaps in the Lyβ Forest at $z < 6$: Evidence of Ultra-late Reionization from XQR-30 Spectra

Yongda Zhu[1], George D. Becker[1], Sarah E. I. Bosman[2], Laura C. Keating[3], Valentina D'Odorico[4,5,6], Rebecca L. Davies[7,8], Holly M. Christenson[1], Eduardo Bañados[2], Fuyan Bian[9], Manuela Bischetti[4], Huanqing Chen[10], Frederick B. Davies[2], Anna-Christina Eilers[11,17], Xiaohui Fan[12], Prakash Gaikwad[2], Bradley Greig[8,13], Martin G. Haehnelt[14], Girish Kulkarni[15], Samuel Lai[16], Andrea Pallottini[5], Yuxiang Qin[8,13], Emma V. Ryan-Weber[7,8], Fabian Walter[2], Feige Wang[12,17], and Jinyi Yang[12,18]
[1] Department of Physics & Astronomy, University of California, Riverside, CA 92521, USA; yzhu144@ucr.edu
[2] Max-Planck-Institut für Astronomie, Königstuhl 17, D-69117 Heidelberg, Germany
[3] Leibniz-Institut für Astrophysik Potsdam (AIP), An der Sternwarte 16, D-14482 Potsdam, Germany
[4] INAF-Osservatorio Astronomico di Trieste, Via Tiepolo 11, I-34143 Trieste, Italy
[5] Scuola Normale Superiore, Piazza dei Cavalieri 7, I-56126 Pisa, Italy
[6] IFPU-Institute for Fundamental Physics of the Universe, via Beirut 2, I-34151 Trieste, Italy
[7] Centre for Astrophysics and Supercomputing, Swinburne University of Technology, Hawthorn, Victoria 3122, Australia
[8] ARC Centre of Excellence for All Sky Astrophysics in 3 Dimensions (ASTRO 3D), Australia
[9] European Southern Observatory, Alonso de Córdova 3107, Casilla 19001, Vitacura, Santiago 19, Chile
[10] Department of Astronomy & Astrophysics, University of Chicago, Chicago, IL 60637, USA
[11] MIT Kavli Institute for Astrophysics and Space Research, 77 Massachusetts Avenue, Cambridge, MA 02139, USA
[12] Steward Observatory, University of Arizona, 933 North Cherry Avenue, Tucson, AZ 85721, USA
[13] School of Physics, University of Melbourne, Parkville, VIC 3010, Australia
[14] Kavli Institute for Cosmology and Institute of Astronomy, Madingley Road, Cambridge, CB3 0HA, UK
[15] Tata Institute of Fundamental Research, Homi Bhabha Road, Mumbai 400005, India
[16] Research School of Astronomy and Astrophysics, Australian National University, Canberra, ACT 2611, Australia
Received 2022 February 25; revised 2022 April 15; accepted 2022 May 9; published 2022 June 17

Abstract

We present a new investigation of the intergalactic medium near reionization using dark gaps in the Lyβ forest. With its lower optical depth, Lyβ offers a potentially more sensitive probe to any remaining neutral gas compared to the commonly used Lyα line. We identify dark gaps in the Lyβ forest using spectra of 42 QSOs at $z_{\rm em} > 5.5$, including new data from the XQR-30 VLT Large Programme. Approximately 40% of these QSO spectra exhibit dark gaps longer than 10 h^{-1} Mpc at $z \simeq 5.8$. By comparing the results to predictions from simulations, we find that the data are broadly consistent both with models where fluctuations in the Lyα forest are caused solely by ionizing ultraviolet background fluctuations and with models that include large neutral hydrogen patches at $z < 6$ due to a late end to reionization. Of particular interest is a very long ($L = 28\ h^{-1}$ Mpc) and dark ($\tau_{\rm eff} \gtrsim 6$) gap persisting down to $z \simeq 5.5$ in the Lyβ forest of the $z = 5.85$ QSO PSO J025−11. This gap may support late reionization models with a volume-weighted average neutral hydrogen fraction of $\langle x_{\rm H\,I} \rangle \gtrsim 5\%$ by $z = 5.6$. Finally, we infer constraints on $\langle x_{\rm H\,I} \rangle$ over $5.5 \lesssim z \lesssim 6.0$ based on the observed Lyβ dark gap length distribution and a conservative relationship between gap length and neutral fraction derived from simulations. We find $\langle x_{\rm H\,I} \rangle \leqslant 0.05$, 0.17, and 0.29 at $z \simeq 5.55$, 5.75, and 5.95, respectively. These constraints are consistent with models where reionization ends significantly later than $z = 6$.

Unified Astronomy Thesaurus concepts: Reionization (1383); Intergalactic medium (813); Quasar absorption line spectroscopy (1317); High-redshift galaxies (734)

Supporting material: data behind figure, figure set

1. Introduction

Determining when and how reionization occurred is essential for understanding the intergalactic medium (IGM) physics and galaxy formation in the early universe (e.g., Muñoz et al. 2022). Recent observations have made significant progress on establishing the timing of reionization and largely point to a midpoint of $z \sim 7$–8. These observations include the electron optical depth to the cosmic microwave background (CMB) photons (Planck Collaboration et al. 2020; see also de Belsunce et al. 2021), the Lyα damping wing in $z \gtrsim 7$ QSO spectra (e.g., Bañados et al. 2018; Davies et al. 2018b; Wang et al. 2020; Yang et al. 2020b; Greig et al. 2022), the decline in observed Lyα emission from $z > 6$ galaxies (e.g., Mason et al. 2018, 2019; Hoag et al. 2019; Hu et al. 2019, and references therein; but see Jung et al. 2020; Wold et al. 2022), and the IGM thermal state measurements at $z > 5$ (e.g., Boera et al. 2019; Gaikwad et al. 2021).

The observations noted above are generally consistent with reionization ending by $z \sim 6$, a scenario supported by existing measurement of the fraction of dark pixels in the Lyman series forests (e.g., McGreer et al. 2011, 2015). Other observations, however, suggest a significantly later end of reionization. The

[17] NASA Hubble Fellow.
[18] Strittmatter Fellow.

large-scale fluctuations in the measured Lyα effective optical depth, $\tau_{\rm eff} = -\ln\langle F\rangle$, where F is the continuum-normalized transmission flux (e.g., Fan et al. 2006; Becker et al. 2015; Eilers et al. 2018; Yang et al. 2020a; Bosman et al. 2022), together with long troughs extending to or below $z \simeq 5.5$ in the Lyα forest (e.g., Becker et al. 2015; Zhu et al. 2021), potentially indicate the existence of large neutral IGM islands (e.g., Kulkarni et al. 2019; Keating et al. 2020b; Nasir & D'Aloisio 2020). The underdensities around long dark gaps traced by Lyα emitters (LAEs) are also consistent with a late reionization model wherein reionization ends at $z < 6$ (Becker et al. 2018; Kashino et al. 2020; Christenson et al. 2021).

These Lyα forest and LAE results are potentially consistent with an alternative scenario wherein the IGM is ionized by $z = 6$ but retains large-scale fluctuations in the ionizing UV background down to lower redshifts (Davies et al. 2018a). On the other hand, recent measurements of the mean free path of ionizing photons measured at $z = 5.1$ and 6.0 (Becker et al. 2021) are difficult to reconcile with models wherein reionization ends at $z > 6$ and may instead prefer models wherein the IGM is still 20% neutral or more at $z = 6$ (Becker et al. 2021; Cain et al. 2021; Davies et al. 2021). In addition, a reionization ending at $z < 6$ is consistent with models that reproduce a variety of observations (e.g., Weinberger et al. 2019; Choudhury et al. 2021; Qin et al. 2021).

One way of searching for signatures of late ($z_{\rm end} < 6$) reionization in the Lyα forest is by investigating dark gaps, i.e., contiguous regions of strong absorption (e.g., Songaila & Cowie 2002; Furlanetto et al. 2004; Paschos & Norman 2005; Fan et al. 2006; Gallerani et al. 2008; Gnedin et al. 2017; Nasir & D'Aloisio 2020). In Zhu et al. (2021, hereafter Paper I), we explored long dark gaps in the Lyα forest and found that a fully ionized IGM with a homogeneous ultraviolet background (UVB) is strongly ruled out down to $z \simeq 5.3$. In contrast, late reionization models and a model wherein reionization ends by $z \sim 6$ but retains large-scale UVB fluctuations are consistent with the observations. Predictions for the Lyα dark gap statistics are similar between the two types of models. This is largely because realistic late reionization models also include UVB fluctuations, which are often associated with the neutral islands. Lyα also tends to saturate at a relatively low ($x_{\rm H\,I} \sim 10^{-3}$) neutral fraction, limiting its sensitivity to neutral gas.

Given its lower optical depth,[19] Lyβ should be a more sensitive probe of neutral gas in the $z \lesssim 6$ IGM. As a result, ultra-late reionization models wherein neutral islands persist down to $z < 5.5$ may produce more long Lyβ dark gaps than can be produced by UVB fluctuations alone. Based on this feature, we can potentially use dark gaps in the Lyβ forest to place stronger constraints on the timing of reionization and distinguish the late reionization models from the pure fluctuating UVB models. As presented in Nasir & D'Aloisio (2020), distributions of dark gaps in the Lyβ forest differ between these models most strongly on scales of $L \gtrsim 10\ h^{-1}$ Mpc. We are therefore particularly interested in these long dark gaps.

In this work, we use 42 high-quality QSO spectra that allow us to search for dark gaps in the Lyβ forest over the redshift range $5.5 < z < 6.0$. The sample includes high-quality X-Shooter spectra from the XQR-30 VLT large program[20] (V. D'Odorico et al. 2022, in preparation). In addition to comparing the results to model predictions, we also constrain $\langle x_{\rm H\,I}\rangle$ based on a conservative relationship between dark gap length and neutral fraction derived from simulations.

This paper is organized as follows. In Section 2 we describe the data and results from the observations. Section 3 compares our results to model predictions, discusses the implications for reionization, and infers constraints on $x_{\rm H\,I}$. Finally, we conclude the findings in Section 4. Throughout this paper, we assume a ΛCDM cosmology with $\Omega_{\rm m} = 0.308$, $\Omega_\Lambda = 0.692$, and $h = 0.678$ (Planck Collaboration et al. 2014). Distances are quoted in comoving units unless otherwise noted.

2. The Data and Results

2.1. QSO Spectra

Our sample includes 42 out of the 43 spectra of QSOs at $5.77 \lesssim z_{\rm em} \lesssim 6.31$ that were used for Paper I. The exception is PSO J004+17, whose spectrum has lower signal-to-noise ratio (S/N) that does not meet the requirement of our flux threshold for the Lyβ forest (Section 2.3). The spectra are taken with the Echellette Spectrograph and Imager (ESI) on Keck (Sheinis et al. 2002) and the X-Shooter spectrograph on the Very Large Telescope (VLT; Vernet et al. 2011). Among these, 19 X-Shooter spectra are from the XQR-30 VLT large program (V. D'Odorico et al. 2022, in preparation). The details of the data reduction procedures are given in Paper I and Becker et al. (2019). We note that the targets are selected without foreknowledge of dark gaps in the Lyβ forest. Figure Set 1 displays the spectra, continuum fits, and dark gaps detected in the Lyβ forest for each QSO (see details below). An example is given in Figure 1.

2.2. Continuum Fitting

We use principal component analysis (PCA) to predict the unabsorbed QSO continuum and normalize the transmission in the Lyβ forest. We follow a similar method to that described in Paper I to fit and predict the continuum. Briefly, we implement and apply the log-PCA method of Davies et al. (2018c) in the Lyα and Lyβ forest portion of the spectrum following Bosman et al. (2022). The continuity between the Lyα forest and the Lyβ forest continuum is broken intentionally to correct for the effect of overlapping Lyα absorption in the Lyβ forest in the PCA training sample. We fit the red-side (rest-frame wavelength $\lambda_0 > 1230$ Å) continuum up to 2000-Å in the rest frame for X-Shooter spectra with NIR observations. The ESI spectra are fit using an optical-only PCA, which is presented in Bosman et al. (2021). The Lyβ dark gap detection is not very sensitive to the continuum, and we also test that using a power-law continuum does not significantly change the dark gap results in this work.

2.3. Dark Gap Detection

Similar to the definition of a dark gap in the Lyα forest in Paper I, we define a dark gap in the Lyβ forest to be a continuous spectral region in which all pixels binned to 1 h^{-1} Mpc have an observed normalized flux $F = F_{\rm obs}/F_c < 0.02$, where $F_{\rm obs}$ is the

[19] Lyβ absorption has a shorter wavelength ($\lambda_{{\rm Ly}\beta} = 1025.72$ Å) and a lower oscillator strength ($f_{{\rm Ly}\beta} = 0.0791$) compared to those of Lyα absorption ($\lambda_{{\rm Ly}\alpha} = 1215.67$ Å, $f_{{\rm Ly}\alpha} = 0.4164$). The ratio of optical depth is given by $\tau_{{\rm Ly}\beta}/\tau_{{\rm Ly}\alpha} = (f_{{\rm Ly}\beta}\lambda_{{\rm Ly}\beta})/(f_{{\rm Ly}\alpha}\lambda_{{\rm Ly}\alpha}) \simeq 0.16$.

[20] https://xqr30.inaf.it

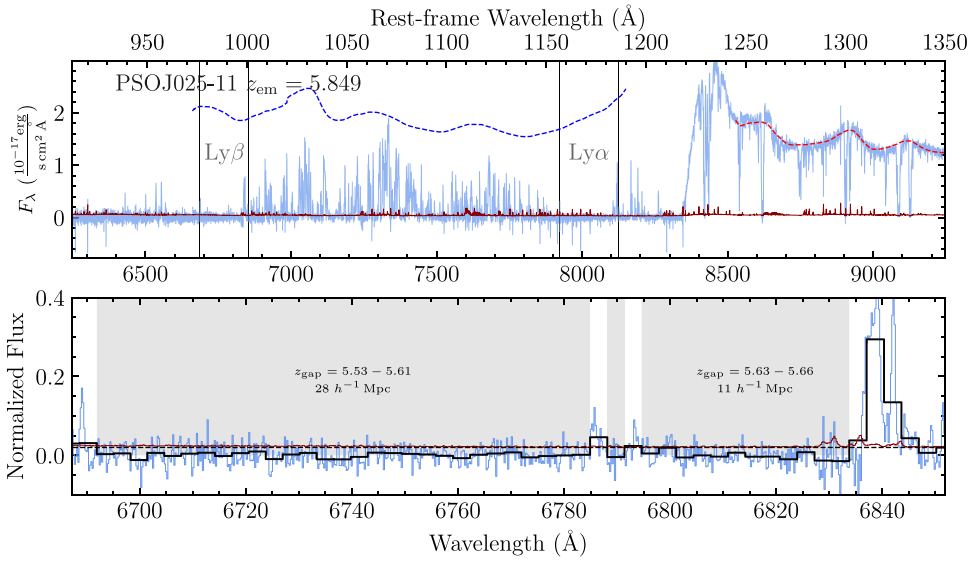

Figure 1. Top panel: spectrum and continuum fits for the $z_{em} = 5.849$ QSO PSO J025−11. The light-blue and dark-red lines represent flux and flux error in the original binning, respectively. Dashed curves redward and blueward of the Lyα peak show the best-fitting and predicted QSO continuum in absence of absorption, respectively. The fitting and prediction are based on PCA. The continuity between the Lyα forest and the Lyβ forest continuum is broken intentionally near 1020 Å in the rest frame. We label the wavelength range over which we search for dark gaps in the Lyβ forest and its corresponding Lyα forest in redshift. Bottom panel: Lyβ forest and dark gaps detected. The dashed black line labels the flux threshold of 0.02. The thick black line displays the flux binned to 1 h^{-1} Mpc. Light-blue and dark-red lines show the flux and flux error in the original binning, respectively. Dark gaps detected are shaded with gray. We also label the redshift range and length of each long ($L \geqslant 10\ h^{-1}$ Mpc) dark gap.

(The complete figure set (42 images) is available.)

observed flux and F_c is the continuum flux. The minimum length of a dark gap is 1 h^{-1} Mpc following Paper I. A bin size of 1 h^{-1} Mpc enables us to retain significant transmission profiles while reducing the influence of very small peaks on dark gap detection. The precise bin size should have relatively little impact on our results provided that the observations and mock spectra are treated consistently. We have verified that using bin sizes of 0.5 h^{-1} Mpc or 1.5 h^{-1} Mpc does not change our major conclusions, although the lengths of some dark gaps would change. A flux threshold of 0.02 is used here instead of 0.05, which we used for the Lyα gaps, because spectra in this subsample have higher S/N levels. In addition, the Lyβ forest at the redshifts that we are interested in is less contaminated by sky lines than the Lyα forest. We have tested that using a threshold of 0.05 will not change our results fundamentally, although the difference between the models (Section 3) may become less significant. In order to reduce false detections caused by foreground Lyα absorption, we further require that all Lyβ dark gaps correspond to Lyα dark gaps as defined in Paper I over the same redshifts for both the observed and mock (Section 3.1) spectra. That is to say, each 1 h^{-1} Mpc bin in the Lyβ dark gap also has a normalized flux less than 0.05 in the Lyα forest at the same redshift.[21] For reference, we present the relationship between Lyβ dark gaps and Lyα dark gaps in Appendix A.

For each QSO sight line, dark gaps are detected from 976 Å in the rest frame to 11 proper-Mpc blueward of the QSO's redshift, which corresponds to approximately 1000 Å in the rest frame. The lower wavelength limit ensures that the detection is not affected by the Lyγ absorption. We use the higher limit to avoid the QSO proximity zone transmission, and the cut is comparable to the choice in, e.g., Bosman et al. (2021). Following Paper I, we also exclude from the statistical analysis an additional 10 h^{-1} Mpc buffer zone blueward of the proximity zone cut. This allows the pixel at the red end of each sight line to intersect a *possible* long ($L \geqslant 10\ h^{-1}$ Mpc) dark gap and hence helps to mitigate potential truncation issues.[22]

To avoid the contamination from sky-line subtraction residuals, we mask out $\pm 75\ km\ s^{-1}$ intervals of the spectra centered at sharp peaks in the flux error array when searching for dark gaps. The exception is that we do not mask transmission with a $>3\sigma$ detection. In addition, we make no attempts to correct for the effects of damped Lyα (DLA) systems or metal-enriched absorbers, although known systems in a subsample of the spectra with a relatively complete identification of metal-enriched systems are discussed in Appendix B. Figure 2 displays an overview of dark gaps detected in the Lyβ forest from our sample.

2.3.1. Dark Gaps Statistics

Figure 3 displays the statistical properties of dark gaps detected in the Lyβ forest from our sample. We detect 195 dark gaps in total, of which 24 have $L \geqslant 10\ h^{-1}$ Mpc. Panel (a) plots length versus central redshift of these dark gaps. Long dark gaps become less common as redshift decreases. Nevertheless, some long gaps still exist down to $z < 5.6$.

We calculate the cumulative distribution function (CDF) of dark gap length, $P(< L)$. Dark gaps are sorted into two redshift

[21] Based on our test, whether requiring gaps to be also dark in the Lyα forest or not only affects a small fraction of gaps and does not change the results in this paper significantly. Although this requirement may not remove all false detection, it partially avoids contamination from random foreground density fluctuations.

[22] Without this additional buffer zone, it is possible that the F_{10} (Section 2.3.1) is underestimated near the red end of a sight line, since there can exist otherwise $\geqslant 10\ h^{-1}$ Mpc gaps that are truncated by the edge or peaks in the proximity zone.

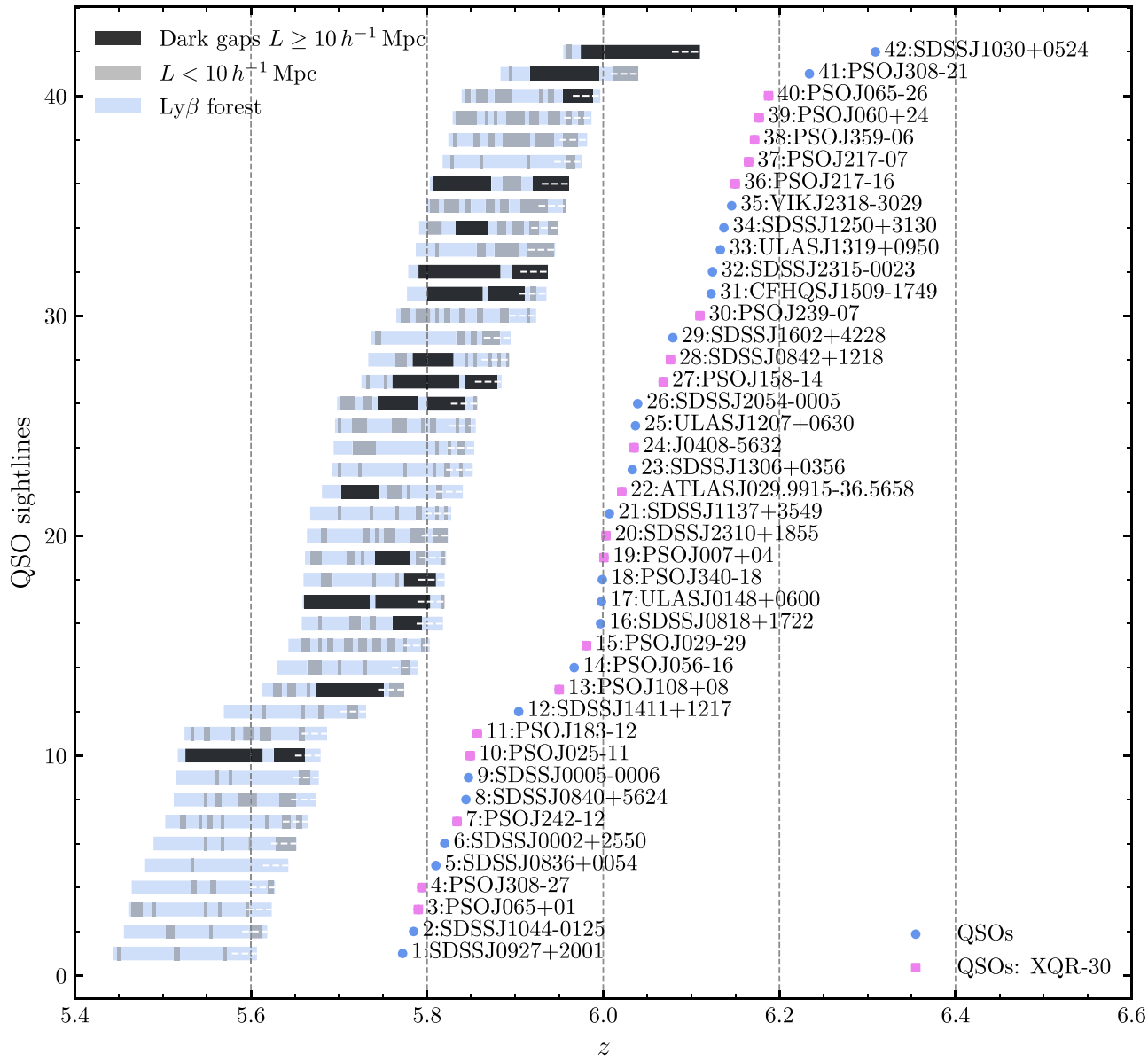

Figure 2. Overview of dark gaps identified in the Lyβ forest from our sample of 42 QSO spectra. Black (gray) bars represent dark gaps longer (shorter) than 10 h^{-1} Mpc. Pink squares label redshifts of XQR-30 targets, and blue circles mark the redshifts of the rest of the QSOs. Light-blue shaded regions demonstrate the redshift coverage of the Lyβ forest. We note that the Lyβ forest is truncated at 11 pMpc from the QSO. The Lyβ forest shown in this figure includes the 10 h^{-1} Mpc buffer zone, labeled with a dashed white line at the red end.

bins according to their redshifts at both ends. For distributions that include dark gaps cut at the red end by the proximity zone limit, we calculate a lower bound on $P(< L)$ by assuming an infinite length for these gaps and an upper bound by assuming that the gap length that would appear in the absence of any proximity effect is the same as the one measured. As shown in Figure 3(b), longer dark gaps become more numerous over $5.75 < z < 6.00$ compared to $5.50 < z < 5.75$. This significant evolution of $P(< L)$ is consistent with the results shown in panel (a).

Following Paper I, we quantify the spatial coverage of large Lyβ-opaque regions by calculating the fraction of QSO spectra showing long ($L \geqslant 10\ h^{-1}$ Mpc) dark gaps as a function of redshift, $F_{10}(z)$. Here we use 10 h^{-1} Mpc as the threshold because dark gaps longer than this in the late reionization models (see Section 3) are dominated by those containing neutral islands. Based on our tests, the number of dark gaps predicted by different models differs the most for $L \gtrsim 10$ h^{-1} Mpc, as also suggested by Nasir & D'Aloisio (2020).

We calculate F_{10} at each redshift and average over $\Delta z = 0.025$ bins. As shown in Figure 3(c), F_{10} has a significant redshift evolution over $5.5 < z < 6.0$. It increases rapidly with redshift over $5.5 < z < 5.8$, from ~10% to ~40%, and climbs up to ~80% by $z = 6.0$ after a drop at $z \sim 5.9$. The reason for the drop is unclear, but the limited number of QSO sight lines may produce large statistical fluctuations (Appendix C), as also shown in the model predictions in Section 3. For comparison, we compute F_{01}, the fraction of QSO sight lines exhibiting dark gaps with $L \geqslant 1\ h^{-1}$ Mpc, and find no significant drop near $z = 5.9$ (see Appendix C).

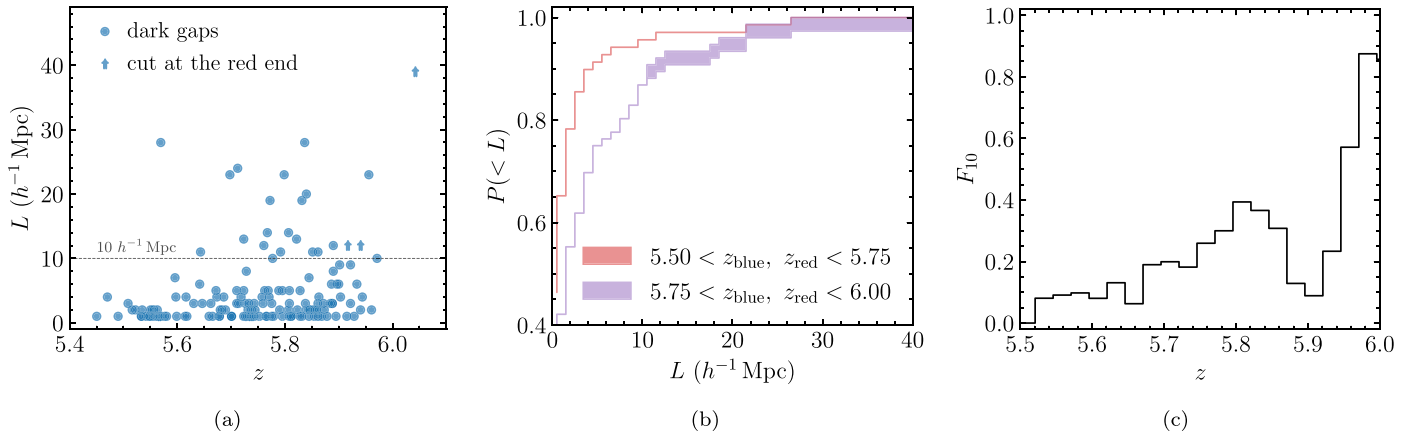

Figure 3. Observed Lyβ dark gaps. (a) Gap length vs. central redshift. Dark gaps cut at the red end by the proximity zone cut are labeled with arrows. (b) Cumulative distribution of dark gap length for two redshift intervals. The upper/lower bounds of the shaded region are described in Section 2.3.1. (c) The fraction of QSO spectra showing dark gaps longer than 10 h^{-1} Mpc as a function of redshift, F_{10}. F_{10} is plotted with a binning of $\Delta z = 0.025$. See text and Appendix C for discussions about the drop of F_{10} near $z = 5.9$.

(The data used to create this figure are available.)

2.3.2. Long Dark Gap toward PSO J025−11

We find a particularly interesting Lyβ gap toward the $z = 5.849$ QSO PSO J025−11 (Figure 1). This dark gap is within the redshift interval of a long (68 h^{-1} Mpc) trough in the Lyα forest. It spans $5.526 \leqslant z \leqslant 5.613$ with a length of 28 h^{-1} Mpc. This is longer and extending to an even lower redshift than the 19 and 23 h^{-1} Mpc Lyβ troughs with $z_{\rm min} = 5.66$ within the extreme (110 h^{-1} Mpc) Lyα trough over $5.523 \leqslant z \leqslant 5.879$ toward ULAS J0148+0600 (Becker et al. 2015). This dark gap toward J025−11 contains no apparent transmission peaks, even in the unbinned data. The 2σ lower limit of $\tau_{\rm eff} \geqslant 6.067$ measured over the complete trough indicates that it is highly opaque.

There is a possibility that part of the trough may be due to either Lyβ or foreground Lyα absorption from the circumgalactic medium (CGM) around intervening galaxies. In this case, corresponding metal lines may be present. We check for potential CGM absorption using the XQR-30 metal absorber catalog (R. L. Davies et al. 2022, in preparation; see Appendix B for technique details). We find no intervening metal systems within the redshift range of the gap. We note that this line of sight has a DLA near the redshift of the QSO, as evidenced by the damping wing at the blue edge of the Lyα proximity zone. The Lyβ gap described here is at a velocity separation of $>3000\,\mathrm{km\,s^{-1}}$ from the QSO, however, and is unaffected by the DLA. The XQR-30 catalog does include a C IV system toward J025−11 at $z = 4.5138$, for which Lyα would fall at the blue end of the Lyβ trough. Overall, however, the general lack of metal absorbers associated with this long dark gap may suggest that the gap probes a low-density region. This would favor the association of highly opaque sight lines with galaxy underdensities, as seen in imaging surveys for galaxies surrounding long Lyα troughs (Becker et al. 2018; Kashino et al. 2020; Christenson et al. 2021).

We examine the possible role of metal-enriched absorbers more broadly in Appendix B, finding little evidence for a strong correlation with long Lyβ troughs. We also examined a sample of lower-redshift lines of sight in Appendix D, finding that metal-enriched absorbers in the foreground Lyα alone are unlikely to create such a long dark gap. We emphasize that this gap falls in redshift within a long Lyα trough spanning $5.461 \leqslant z \leqslant 5.674$ with $L = 68\ h^{-1}$ Mpc that does not appear to be affected by metal absorbers (Paper I). This combination of factors gives us confidence that the $L = 28\ h^{-1}$ Mpc dark gap is genuinely caused by IGM opacity.[23]

3. Models and Discussion

3.1. Models and Mock Spectra

Here we compare our results to predictions from models based on hydrodynamical simulations. We use the following models, which were also used in Paper I:

1. the `homogeneous-UVB` model from the Sherwood Simulation Suite (Bolton et al. 2017), which uses a homogeneous Haardt & Madau (2012) UV background;
2. late reionization models wherein reionization ends at $z \lesssim 5.3$, including `K20-low-`$\tau_{\rm CMB}$, `K20-low-`$\tau_{\rm CMB}$`-hot`, and `K20-high-`$\tau_{\rm CMB}$ models from Keating et al. (2020a) and `ND20-late-longmfp` and `ND20-late-shortmfp` models from Nasir & D'Aloisio (2020); and
3. an early reionization model wherein the IGM is mostly ionized by $z = 6$ but large-scale fluctuations in the UVB, which are amplified by a short mean free path of ionizing photons ($\lambda_{\rm mfp}^{912} = 10 h^{-1}$ Mpc at $z = 5.6$), persist down to lower redshifts (`ND20-early-shortmfp`; Nasir & D'Aloisio 2020).

These models were chosen, in part, because they reproduce at least some other observations of the Lyα forest. The `homogeneous-UVB` model agrees well with observations at $z < 5$ including the IGM temperature and flux power spectra (Bolton et al. 2017), although it fails to predict the Lyα opacity distribution at $z > 5$ (e.g., Bosman et al. 2022). The late reionization and fluctuating UVB models are broadly consistent with observations of IGM temperature, mean Lyα transmission, and fluctuations in Lyα opacity over the redshift range we

[23] In an extreme case where this foreground absorber links two shorter dark gaps, although very unlikely, one of these two shorter dark gaps would still have a size of $L \sim 25\ h^{-1}$ Mpc.

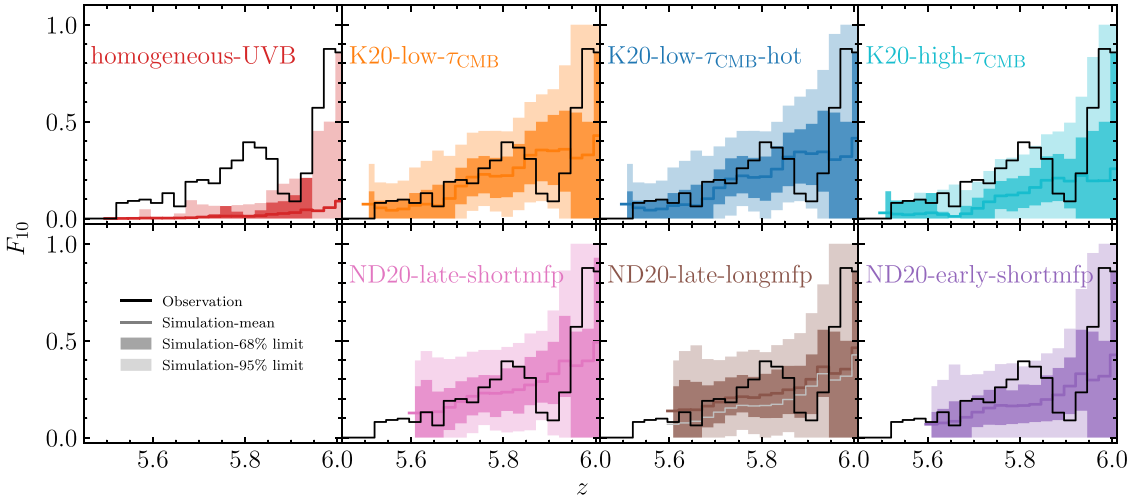

Figure 4. Fraction of QSO spectra showing long ($L \geqslant 10\ h^{-1}$ Mpc) Lyβ dark gaps as a function of redshift predicted by different models. The colored lines, dark-shaded regions, and light-shaded regions show the mean, 68% limit, and 95% limit of F_{10} predicted by models based on 10,000 realizations. The black lines plot F_{10} from the observations. For comparison, we also overplot the mean F_{10} predicted by the `ND20-early-shortmfp` in the panel of the `ND20-late-longmfp` model with a gray line.

are interested in (Keating et al. 2020a; Nasir & D'Aloisio 2020). Moreover, these models are able to produce long Lyα troughs at $z < 6$ (e.g., Paper I). We note, nevertheless, that none of the models we use can self-consistently predict the mean free path evolution over $5 < z < 6$ as measured in Becker et al. (2021).

In the `homogeneous-UVB` model, the IGM is instantaneously reionized at $z = 15$. At $z < 6$, therefore, the IGM in this model is fully ionized and the gas is hydrodynamically relaxed. A homogeneous-UVB model that produced a later reionization (e.g., Puchwein et al. 2019; Villasenor et al. 2021) would mainly alter the temperature and pressure smoothing at $z < 6$. These are small-scale effects, however, that should only minimally impact our measurements. We would generally expect that any homogeneous-UVB model that reionizes by $z = 6$ would produce similar dark gap statistics to the Haardt & Madau (2012) UVB once the ionization rates at $z < 6$ are rescaled to reproduce the observed mean flux.

The `K20-low-`$\tau_{\rm CMB}$`-hot` model shares a similar reionization history with the `K20-low-`$\tau_{\rm CMB}$ model, but it has a different thermal history with a volume-weighted mean temperature at the mean density at $z = 6$ of $T_0 = 10{,}000$ K, compared to that of the latter being 7000 K. The `K20-high-`$\tau_{\rm CMB}$ model has an earlier midpoint of reionization at $z = 8.4$, which is at the upper end of the value suggested by CMB measurements (Planck Collaboration et al. 2020). As for the late reionization models from Nasir & D'Aloisio (2020), the main difference is that the `ND20-late-shortmfp` model includes stronger post-reionization UVB fluctuations than the `ND20-late-longmfp` model, while they both have neutral islands surviving at $z < 6$. The mean free paths of ionizing photons at $z = 5.6$ in these two models are $\lambda_{\rm mfp}^{912} = 10$ and 30 h^{-1} Mpc, respectively.

The box sizes we use in this work are $L = 160$, 160, and 200 h^{-1} Mpc for simulations in Bolton et al. (2017), Keating et al. (2020a), and Nasir & D'Aloisio (2020), respectively. We note that the `K20` models are from radiative transfer simulations run in post-processing and that the `ND20` models are seminumeric models. For more details on the models, see Paper I.

We rescale the optical depths in the simulations as needed in order to match the observed mean flux in the Lyα forest (see, e.g., Section 2.2 in Bolton et al. 2017, and references therein). We scale to the measurements of Bosman et al. (2018), which are consistent with the mean Lyα fluxes obtained from our sample. The same rescaling factor is then applied to both the Lyα and corresponding Lyβ optical depths. We note that this rescaling mainly applies to the `homogeneous-UVB` model, for which scaling by factors of $\sim$0.4–0.6 is required over $5 < z < 6$. We are therefore explicitly testing only a `homogeneous-UVB` model that also matches the observed mean Lyα flux. The Keating et al. (2020a) models already produce a mean Lyα transmission consistent with the measurements of Bosman et al. (2018). The mock spectra from this simulation are continuous in redshift, with a smoothly evolving mean flux. Nasir & D'Aloisio (2020) also calibrated their simulations to the observed $\tau_{\rm eff}$ from Bosman et al. (2018) but provide one-dimensional skewers at discrete redshifts. For these simulations we therefore only need to rescale the optical depths such that the mock spectra described below have a mean flux that evolves smoothly with redshift.

We derive dark gap predictions from forward-modeled mock spectra that are matched to the observed sample in QSO redshift, resolution, and S/N. Keating et al. (2020a) provide mock spectra of the Lyβ forest including the foreground Lyα absorption. For the `homogeneous-UVB` model and models from Nasir & D'Aloisio (2020) we follow the methods described in Paper I to build the mock Lyβ forest and foreground Lyα forest. In all cases we rebin the mock spectra and apply the noise arrays according to each observed spectrum.

3.2. Model Comparisons

3.2.1. Comparisons of F_{10}

We compute the predicted F_{10} of each model based on 10,000 randomly selected sets of mock spectra of the same size as the observed sample. Their mean, 68% limit, and 95% limit are plotted in Figure 4, along with the observations. Similar to F_{30}[24] for the Lyα forest in Paper I, F_{10} shows jagged features

[24] F_{30} is defined as the fraction of QSO spectra exhibiting gaps longer than 30 h^{-1} Mpc as a function of redshift.

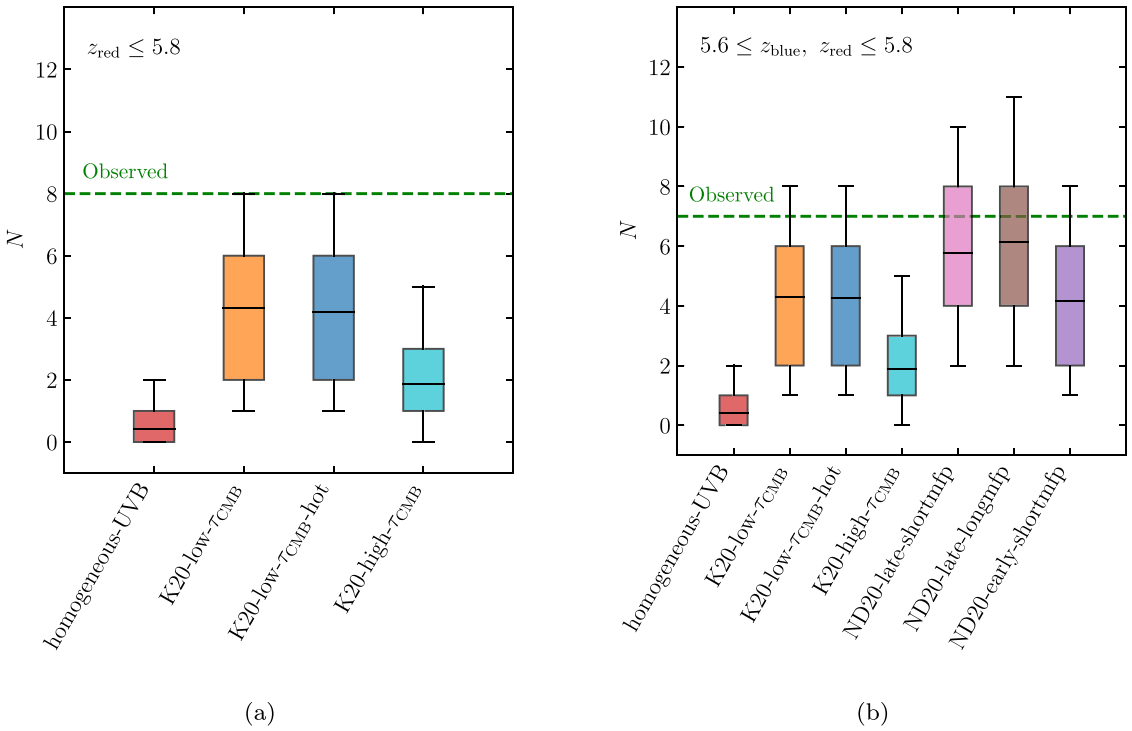

Figure 5. (a) Number of long ($L \geqslant 10\ h^{-1}$ Mpc) Lyβ dark gaps that lie entirely below $z = 5.8$ in the mock sample from each model. (b) Number of long dark gaps entirely over $5.6 \leqslant z \leqslant 5.8$. In both panels the center lines, boxes, and error bars show the mean, 68% limit, and 95% limit, respectively. The observed numbers of long dark gaps in each redshift range are indicated by dashed green lines.

due to the combined effects of step changes in the number of sight lines with redshift and the quantization of F_{10} for a finite sample size. We note that 68th and 95th percentile limits can share their upper and/or lower bounds at some redshifts, for the same reason. These features, on the other hand, show the constraining ability of the current sample size and data quality. The drop at $z \sim 5.9$ seen in the observed F_{10} is also broadly included in the 95% limits for most of the models.

The `homogeneous-UVB` model is not supported by the data at the $\geqslant$95% level. This is consistent with the conclusion based on the Lyα forest in Paper I that a fully ionized IGM with a homogeneous-UVB scenario is disfavored by the data at $z < 6$ down to $z \simeq 5.3$. In contrast, the late reionization models are still consistent with the data, except for the `K20-high-`$\tau_{\rm CMB}$ model, which covers the observed F_{10} just within its 95% upper limit. This supports the conclusion of Paper I that this extended reionization model is less favored by the data owing to its insufficient neutral hydrogen and/or UVB fluctuations at $z < 6$.

Our results further show that dark gaps in Lyβ are more sensitive probes of neutral regions than gaps in Lyα. For dark gaps in the Lyα forest, we see little difference between the `ND20-early-shortmfp` model and the `ND20-late` models (Paper I). In the Lyβ forest, however, the former predicts a smaller F_{10} than the latter by $\sim$0.05 at most redshifts. This difference is not enough for us to distinguish them based on the current sample, although the Lyβ gaps put some pressure on the early reionization model. Nasir & D'Aloisio (2020) note that these models are different in their Lyβ dark gap length distributions, while they cannot be distinguished in the Lyα forest. Nevertheless, we compute the differential dark gap length distribution for individual ΔL bins, $L\Delta P(L)/\Delta L$, and find that their differences are minor compared to the scatter of the data. Looking ahead to the era of Extremely Large Telescopes, we forecast that $\sim$100 lines of sight with the Lyβ forest covering $z \sim 5.8$ would be needed to distinguish the two models at $\sim$95% confidence based on F_{10}. An S/N of 50 per 10 km s^{-1} for the spectra would be adequate according to our tests using mock spectra.

3.2.2. Total Number of Long Dark Gaps at z ⩽ 5.8

To further illustrate the differences between models, we use our mock data to calculate the total number of long dark gaps predicted to lie entirely at $z < 5.8$. Figure 5 compares the model results to the observations. Given that the `ND20` models only have outputs down to $z = 5.6$, we exclude these models when counting the total number of long dark gaps below $z = 5.8$. We nevertheless include the `ND20` models for dark gaps that fall entirely over $5.6 \leqslant z \leqslant 5.8$ for reference.

The results are consistent with those from F_{10}. As shown in Figure 5(a), the 95% upper limit of the predicted number of long dark gaps by the `homogeneous-UVB` model is 2. This is a factor of 4 smaller than the observed value, which is 8. The `K20-high-`$\tau_{\rm CMB}$ model is also disfavored by the data at >95% confidence given its deficit of long dark gaps. In contrast, the rapid late reionization models, i.e., `K20-low-`$\tau_{\rm CMB}$ models, agree with the observations within their 95% limits.

Over $5.6 \leqslant z \leqslant 5.8$ the observed number of long dark gaps decreases by 1 while the simulation predictions show little change. In this case, rapid late reionization models from Keating et al. (2020a) are still consistent with the data. The observations also support both fluctuating UVB and late reionization models from Nasir & D'Aloisio (2020). We note that the difference between the predicted mean numbers and the observed value is smallest for the `ND20-late` models, wherein $\langle x_{\rm H\,I} \rangle$ is still higher than $\sim$5% by $z = 5.6$. On the

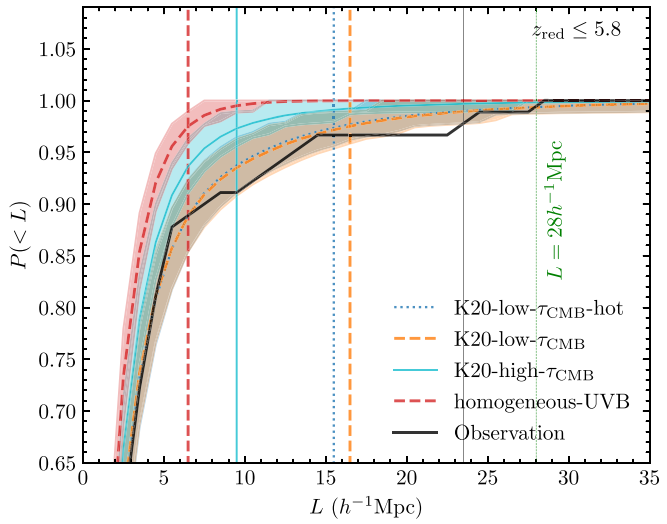

Figure 6. Cumulative distribution of dark gaps that are entirely below $z = 5.8$. Vertical colored lines indicate the 97.5% limit for each model. The color shaded regions plot the 68% limit for each model. From left to right are the `homogeneous-UVB` model, the `K20-high-`$\tau_{\rm CMB}$ model, and the `K20-low-`$\tau_{\rm CMB}$`-hot` model (almost completely overlapped with the `K20-low-`$\tau_{\rm CMB}$ model).

other hand, the `K20-high-`$\tau_{\rm CMB}$ model is disfavored by the data also in this redshift range. This would suggest that very extended reionization scenarios in which insufficient neutral hydrogen and/or UVB fluctuations remain at $z < 6$ may be disfavored.

3.2.3. Detection Rate of an $L \geqslant 28$ h^{-1} Mpc Dark Gap

Perhaps the most conspicuous feature in the observations is the $L = 28$ h^{-1} Mpc dark gap toward PSO J025−11 that extends down to $z \simeq 5.5$. The appearance of this gap may indicate that significant neutral hydrogen islands and/or UVB fluctuations persist down to $z \simeq 5.5$ and provide further leverage for discriminating between models. As the outputs of the `ND20` models have no redshift coverage for this dark gap, we only compare the `K20` models and the `homogeneous-UVB` model for this section.

For each model, we use 10,000 bootstrapping realizations to calculate the CDF of dark gap length, $P(<L)$. Figure 6 compares the observed and predicted $P(<L)$ for dark gaps that are entirely below $z = 5.8$. As indicated by the vertical lines, the observed dark gap with $L = 28$ h^{-1} Mpc is well beyond the 95% limits of all the models shown here. These results suggest that the $L = 28$ h^{-1} Mpc gap we observed in the Lyβ forest toward PSO J025−11 is extremely rare in these models. We perform Mann−Whitey U tests (Mann & Whitney 1947) for the hypotheses that the distributions of L in the data and predicted by models are equal, for each model respectively. The hypothesis is rejected with p-values <0.05 for the `homogeneous-UVB` model.

We further calculate the detection rate of at least one $L = 28$ h^{-1} Mpc gap entirely below $z = 5.61$ in the mock samples from each model with the required redshift coverage. We note that in the data there are 10 QSO spectra where the Lyβ forest (excluding the proximity zone) covers the full central redshift range of the $L = 28$ h^{-1} Mpc dark gap. We find zero detections of such long dark gaps in the `homogeneous-UVB` model out of 10,000 trails. The `K20-high-`$\tau_{\rm CMB}$ model yields a detection rate of 4%. Both the `K20-low-`$\tau_{\rm CMB}$ and `K20-low-`$\tau_{\rm CMB}$`-hot` models give a higher detection rate of 10%. These results suggest that in the case of a late reionization, models with a volume-weighted average neutral hydrogen fraction $\langle x_{\rm H\,I}\rangle \gtrsim 5\%$ at $z = 5.6$ are more consistent with the observations. In addition, the relatively rare presence of $L \geqslant 28$ h^{-1} Mpc gaps in the models could also be related to the size of the simulation volume (160 h^{-1} Mpc for the `K20` simulations). Simulations run in larger volumes may be needed to compute more accurate statistics on the incidence of these rare, long troughs in late reionization models.

3.3. Neutral Hydrogen Fraction

We can further use dark gaps to infer an upper limit on $\langle x_{\rm H\,I}\rangle$. One can set a strict upper limit on the neutral fraction by assuming that all dark gaps correspond to neutral gas (e.g., McGreer et al. 2011, 2015). At the end of reionization, however, a combination of density and UVB fluctuations will tend to produce dark gaps even once the gas is ionized. We therefore wish to use insights from reionization models to derive a more physically motivated but still conservative upper limit on $\langle x_{\rm H\,I}\rangle$ from the covering fraction of dark gaps. As described below, we use the fact that dark gaps in the late reionization models tend to show a correlation between the volume-averaged neutral fraction within a gap and the gap length. By applying this relationship to the observed gap length distribution, we can set constraints on $\langle x_{\rm H\,I}\rangle$.

Our goal is to set physically reasonable constraints on $\langle x_{\rm H\,I}\rangle$ while minimizing the model dependency. We therefore wish to identify the maximum average neutral fraction for a given gap length that is allowed by the models. We first explore the distribution of neutral fractions for a given dark gap length, $f(x_{\rm H\,I}|L)$. We focus on two models wherein neutral regions contribute significantly to forming dark gaps, the `ND20-late-longmfp` model and the `K20-low-`$\tau_{\rm CMB}$ model. Using the mock data, we calculate $x_{\rm H\,I}$ for each dark gap by averaging the neutral fraction pixel-wise. Figure 7(a) plots the mean neutral fraction of dark gaps as a function of length, $\langle x_{\rm H\,I}\rangle_L$, at different redshifts. It is related to $f(x_{\rm H\,I}|L)$ by

$$\langle x_{\rm H\,I}\rangle_L = \int_0^1 x_{\rm H\,I} f(x_{\rm H\,I}|L) dx_{\rm H\,I}. \quad (1)$$

As shown in the figure, dark gaps of a given length tend to be more neutral as redshift decreases. This is largely because the opacity of the ionized IGM tends to decrease with decreasing redshift, making it more difficult to produce long gaps through density and/or UVB fluctuations alone. In order to set conservative upper limits of $\langle x_{\rm H\,I}\rangle$, we adopt the $\langle x_{\rm H\,I}\rangle_L$ relationship from `ND20-late-longmfp` at $z = 5.6$. The normalized $f(x_{\rm H\,I}|L)$ for each dark gap length interval is plotted in Figure 7(b). This is similar to but slightly higher than the relationship from `K20-low-`$\tau_{\rm CMB}$ at the same redshift. We also note that the redshift evolution in $\langle x_{\rm H\,I}\rangle_L$ in these models is relatively modest, up to a factor of $\sim$2 in the `K20-low-`$\tau_{\rm CMB}$ model between $z \sim 6$ and 5.6.

In order to translate the observed gap length distribution into an $\langle x_{\rm H\,I}\rangle$ constraint, we calculate $\mathscr{F}_L$, the fraction of QSO spectra showing dark gaps with length L as a function of redshift. At a certain redshift, the total mean neutral hydrogen

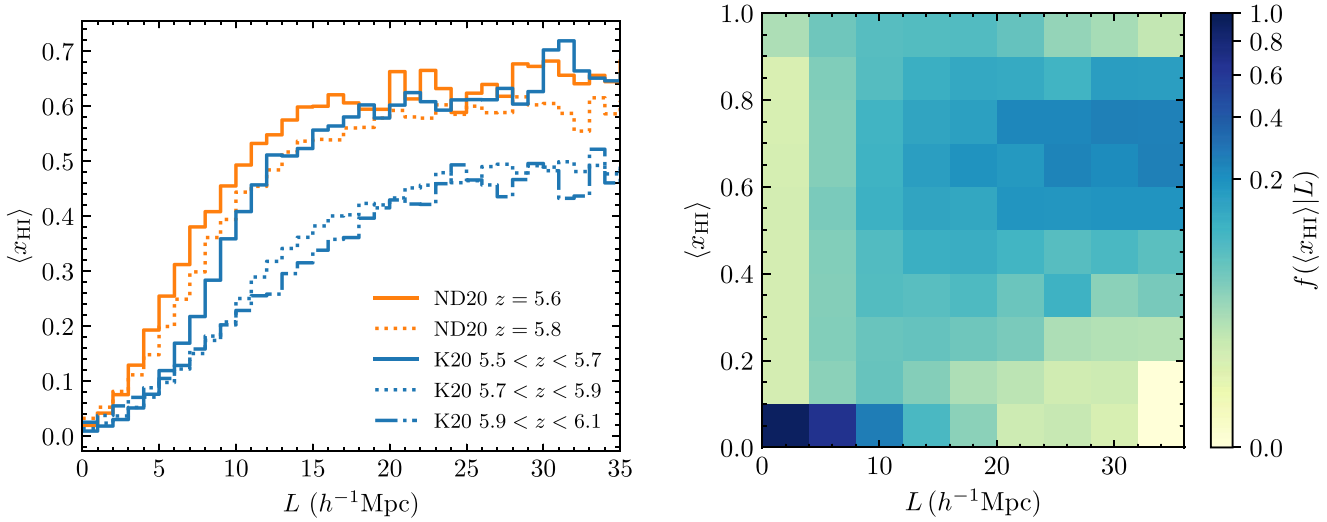

Figure 7. (a) The mean volume-weighted neutral fraction ($\langle x_{\rm H\,I} \rangle$) over a Ly$\beta$ dark gap for a given dark gap length in the mock data. In this figure, "ND20" and "K20" refer to the `ND20-late-longmfp` model and the `K20-low-`$\tau_{\rm CMB}$ model, respectively. (b) Distribution of $\langle x_{\rm H\,I} \rangle$ for a given Lyβ dark gap length, $f(x_{\rm H\,I}|L)$, in the `ND20-late-longmfp` model at $z = 5.6$; $f(x_{\rm H\,I}|L)$ is normalized for each L interval.

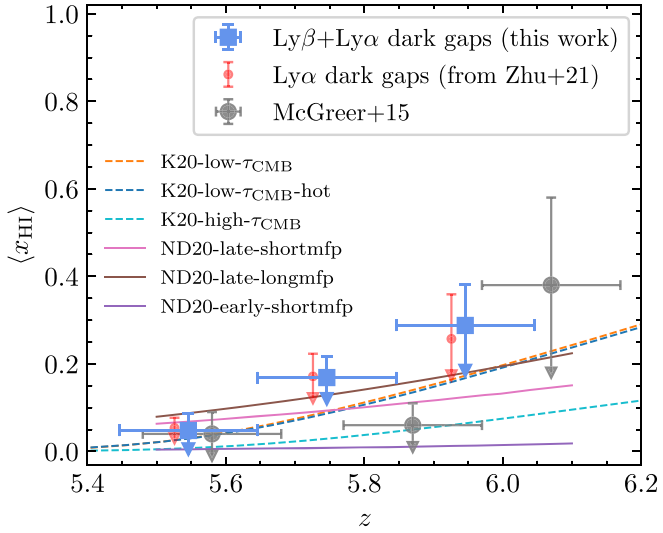

Figure 8. Inference on the neutral hydrogen fraction ($\langle x_{\rm H\,I} \rangle$) from Ly$\beta$ dark gaps, which are also dark in the Lyα forest by definition. We show constraints based on Lyα dark gaps from Paper I with red error bars, which are shifted by -0.02 in redshift for display. Gray markers plot the constraints based on fraction of pixels that are dark in both the Lyα and Lyβ forests from McGreer et al. (2015). The vertical error bars show the 68% (1σ) limits. The horizontal error bars indicate the $\Delta z = 0.2$ redshift bins. For reference, colored lines plot the redshift evolution of $\langle x_{\rm H\,I} \rangle$ for the reionization models used in this work.

fraction is then given by

$$\langle x_{\rm H\,I} \rangle = \sum_{L=1}^{\infty} \mathscr{F}_L \langle x_{\rm H\,I} \rangle_L . \quad (2)$$

Here we use a sum for L instead of an integral because we measure dark gap lengths in increments of 1 h^{-1} Mpc. To estimate the uncertainty in $\langle x_{\rm H\,I} \rangle$, we randomly select the observed sight lines with replacement and calculate the corresponding $\mathscr{F}_L$. We use bootstrapping to randomly sample the neutral hydrogen fraction from $f(x_{\rm H\,I}|L)$ given by models and multiply by the observed $\mathscr{F}_L$ of this sample, and then we sum up for all dark gap lengths. The final uncertainty in $\langle x_{\rm H\,I} \rangle$ is calculated by repeating this process 10,000 times.

The results are shown in Figure 8. We calculate $\langle x_{\rm H\,I} \rangle$ in Equation (2) over $\Delta z = 0.2$ bins. The inferred upper limits on $\langle x_{\rm H\,I} \rangle$ are $0.05^{+0.04}_{-0.04}$, $0.17^{+0.05}_{-0.05}$, and $0.29^{+0.09}_{-0.10}$ at $z \simeq 5.55$, 5.75, and 5.95, respectively. We also calculate $\langle x_{\rm H\,I} \rangle$ following the same method based on Lyα dark gaps presented in Paper I, as shown with red symbols in Figure 8. The Lyα dark gaps yield $\langle x_{\rm H\,I} \rangle \leqslant 0.05$, 0.17, and 0.26 at $z \simeq 5.55$, 5.75, and 5.95, respectively. The measurements based on Lyα and Lyβ dark gaps are highly consistent with each other. Compared to the measurements based on the fraction of dark pixels by McGreer et al. (2015), our results potentially allow a higher neutral fraction over $5.6 \lesssim z \lesssim 6.0$ and a later reionization. The difference in $\langle x_{\rm H\,I} \rangle$ might be due to cosmic variance and/or the different definitions of dark gaps and dark pixels used in these works. The $\langle x_{\rm H\,I} \rangle$ measurement at $z \sim 5.9$ in McGreer et al. (2015), moreover, may be biased by transmission peaks in the QSO proximity zone given that their wavelength range for both the Lyα and Lyβ forests ends at $z_{\rm QSO} - 0.1$, which is less than 6.5 pMpc from the QSO at $z \sim 6$ (see proximity zone size measurements in, e.g., Eilers et al. 2017, 2020).

4. Conclusion

In this work, we explore the IGM near the end of reionization using dark gaps in the Lyβ forest over $5.5 \lesssim z \lesssim 6.0$. We show that about 10%, 40%, and 80% of QSO spectra exhibit long ($L \geqslant 10\ h^{-1}$ Mpc) dark gaps in their Lyβ forest at $z \simeq 5.6$, 5.8, and 6.0, respectively. Among these gaps, we detect a very long ($L = 28\ h^{-1}$ Mpc) and dark ($\tau_{\rm eff} \gtrsim 6$) Lyβ gap extending down to $z \sim 5.5$ toward the $z_{\rm em} = 5.85$ QSO PSO J025−11.

A comparison between the observed Lyβ dark gap statistics for the whole sample of 42 lines of sight and predictions from multiple reionization models (Bolton et al. 2017; Keating et al. 2020a; Nasir & D'Aloisio 2020) confirms that evidence of reionization in the form of neutral islands and/or a fluctuating

UV background persists down to at least $z \sim 5.5$. This supports the conclusions in Paper I and Bosman et al. (2022). In Paper I we noted a possible tension between Lyα gap statistics and a model wherein reionization ends by $z < 6$ but has a relatively early midpoint of $z = 8.4$ (Keating et al. 2020a). With Lyβ this tension becomes more significant (>95% level) based on the count of long dark gaps at $z \leqslant 5.8$, suggesting that very extended reionization scenarios with insufficient remaining neutral hydrogen and/or UVB fluctuations at $z < 6$ may be disfavored. In contrast, rapid late reionization models with $\langle x_{\rm H\,I} \rangle \gtrsim 5\%$ at $z = 5.6$ (Keating et al. 2020a; Nasir & D'Aloisio 2020) are consistent with the observations. A model wherein reionization ends early but retains large-scale fluctuations in the ionizing UV background (Nasir & D'Aloisio 2020) is also permitted by the dark gap data. We note, however, that recent IGM temperature measurements from Gaikwad et al. (2020) disfavor this model.

A caveat is that we are testing only specific reionization models, including only one with a fluctuating UVB in which reionization ends at $z > 6$. By comparison, Gnedin et al. (2017) showed that their full radiative transfer simulations, which reionized near $z \sim 7$, were able to reproduce the Lyα dark gap distribution measured from ESI spectra of a set of 12 $z \sim 6$ QSOs. Because Lyβ dark gaps are correlated with Lyα opacities (Appendix A), it is possible that some early reionization scenarios with UVB fluctuations can reproduce our Lyβ dark gap distributions while also matching the observed evolution of the mean Lyα transmission.

Finally, we use the observed Lyβ gaps to place constraints on the neutral hydrogen fraction based on the association between neutral islands and dark gaps seen in reionization simulations. Our results are broadly consistent with, but more permissive than, the constraints from McGreer et al. (2011, 2015) that are based on the dark pixel fraction. Notably, we find an upper limit at $z \simeq 5.75$ of $\langle x_{\rm H\,I} \rangle \leqslant 0.17$. This constraint is consistent with scenarios wherein reionization extends significantly below $z = 6$.

We thank Elisa Boera and Fahad Nasir for their help with simulated data and for useful discussions. We also thank the anonymous referee for their constructive comments.

Y.Z., G.D.B., and H.M.C. were supported by the National Science Foundation through grants AST-1615814 and AST-1751404. H.M.C. was also supported by the National Science Foundation Graduate Research Fellowship Program under grant No. DGE-1326120. S.E.I.B. and F. Walter acknowledge funding from the European Research Council (ERC) under the European Union's Horizon 2020 research and innovation program (grant agreement No. 740246 "Cosmic Gas"). L.C.K. was supported by the European Union's Horizon 2020 research and innovation program under the Marie Sklodowska-Curie grant agreement No. 885990. M.B. acknowledges support from PRIN MIUR project "Black Hole Winds and the Baryon Life Cycle of Galaxies: The Stone-guest at the Galaxy Evolution Supper," contract No. 2017PH3WAT. F.B. acknowledges support from the Australian Research Council through Discovery Projects (award DP190100252) and Chinese Academy of Sciences (CAS) through a China-Chile Joint Research Fund (CCJRF1809) administered by the CAS South America Center for Astronomy (CASSACA). H.C. thanks the support by NASA through the NASA FINESST grant NNH19ZDA005K. A.-C.E. acknowledges support by NASA through the NASA Hubble Fellowship grant No. HF2-51434 awarded by the Space Telescope Science Institute, which is operated by the Association of Universities for Research in Astronomy, Inc., for NASA, under contract NAS5-26555. X.F. and J.Y. acknowledge support from the NSF grants AST 115-15115 and AST 19-08284. M.G.H. acknowledges support from the UKRI STFC (grant Nos. ST/N000927/1 and ST/S000623/1). G.K.'s research is partly supported by the Max Planck Society via a partner group grant. A.P. acknowledges support from the ERC Advanced Grant INTERSTELLAR H2020/740120. Parts of this work were supported by the Australian Research Council Centre of Excellence for All Sky Astrophysics in 3 Dimensions (ASTRO 3D), through project No. CE170100013. F. Wang thanks the support provided by NASA through the NASA Hubble Fellowship grant No. HST-HF2-51448.001-A awarded by the Space Telescope Science Institute, which is operated by the Association of Universities for Research in Astronomy, Incorporated, under NASA contract NAS5-26555.

Based on observations collected at the European Southern Observatory under ESO programmes 060.A-9024(A), 084.A-0360(A), 084.A-0390(A), 084.A-0550(A), 085.A-0299(A), 086.A-0162(A), 086.A-0574(A), 087.A-0607(A), 088.A-0897(A), 091.C-0934(B), 096.A-0095(A), 096.A-0418(A), 097.B-1070(A), 098.A-0111(A), 098.B-0537(A), 0100.A-0243(A), 0100.A-0625(A), 0101.B-0272(A), 0102.A-0154(A), 0102.A-0478(A), 1103.A-0817(A), and 1103.A-0817(B).

Some of the data presented herein were obtained at the W. M. Keck Observatory, which is operated as a scientific partnership among the California Institute of Technology, the University of California, and the National Aeronautics and Space Administration. The Observatory was made possible by the generous financial support of the W. M. Keck Foundation. The authors wish to recognize and acknowledge the very significant cultural role and reverence that the summit of Maunakea has always had within the indigenous Hawaiian community. We are most fortunate to have the opportunity to conduct observations from this mountain. Finally, this research has made use of the Keck Observatory Archive (KOA), which is operated by the W. M. Keck Observatory and the NASA Exoplanet Science Institute (NExScI), under contract with the National Aeronautics and Space Administration.

This work was performed using the Cambridge Service for Data Driven Discovery (CSD3), part of which is operated by the University of Cambridge Research Computing on behalf of the STFC DiRAC HPC Facility (www.dirac.ac.uk). The DiRAC component of CSD3 was funded by BEIS capital funding via STFC capital grants ST/P002307/1 and ST/R002452/1 and STFC operations grant ST/R00689X/1. This work further used the DiRAC@Durham facility managed by the Institute for Computational Cosmology on behalf of the STFC DiRAC HPC Facility. The equipment was funded by BEIS capital funding via STFC capital grants ST/P002293/1 and ST/R002371/1, Durham University, and STFC operations grant ST/R000832/1. DiRAC is part of the National e-Infrastructure.

Facilities: Keck:II (ESI), VLT:Kueyen (X-Shooter).

Software: `Astrocook` (Cupani et al. 2020), `Astropy` (Astropy Collaboration et al. 2013), `Matplotlib` (Hunter 2007), `NumPy` (van der Walt et al. 2011), `SpectRes` (Carnall 2017).

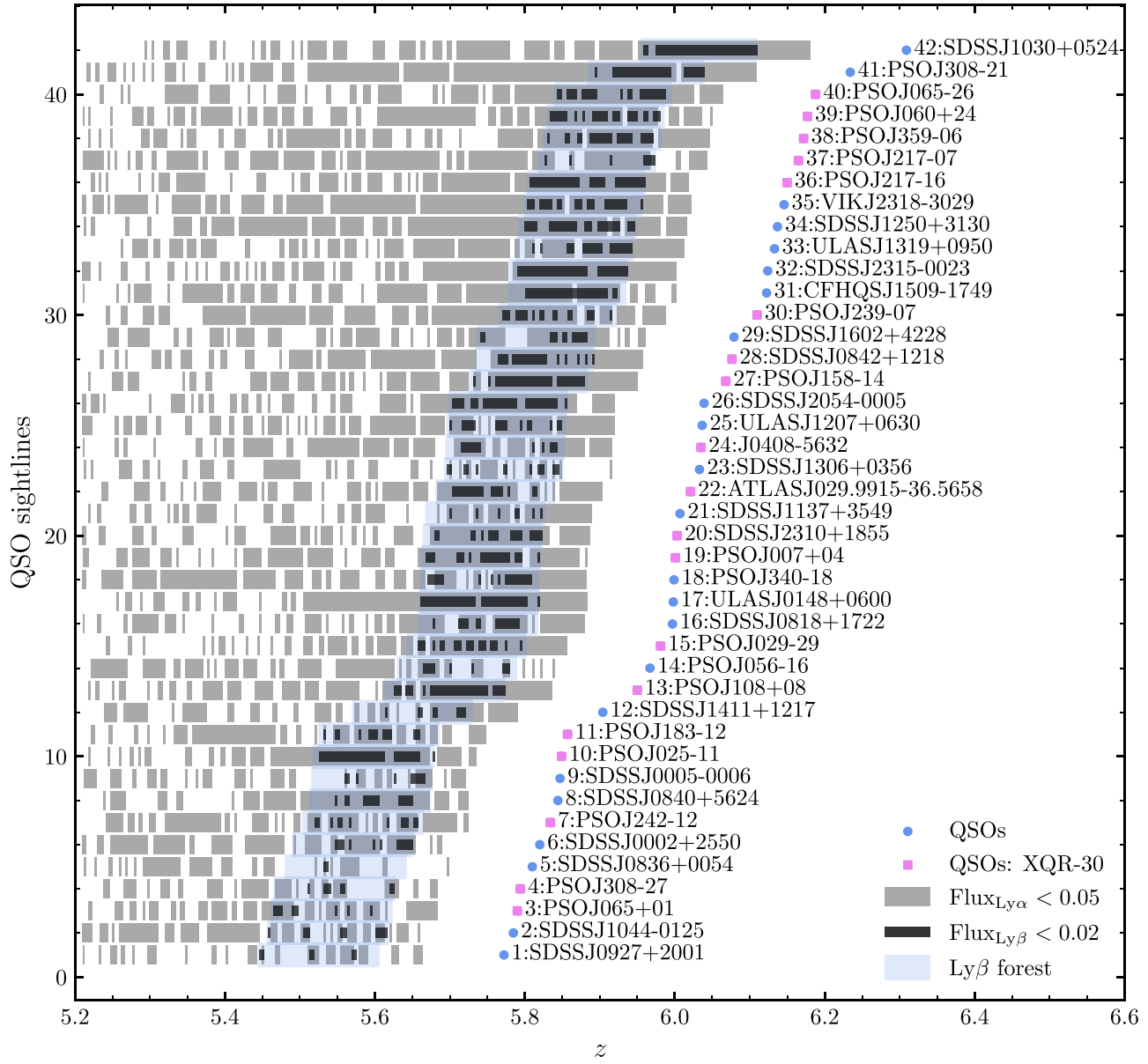

Figure A1. Overview of Lyβ-opaque regions and Lyα dark gaps from our sample of 42 QSO lines of sight. Black bars show Lyβ-opaque regions, where normalized flux in the Lyβ forest Flux$_{Ly\beta} < 0.02$ per 1 h^{-1} Mpc bin. Gray bars show Lyα dark gaps as defined in Paper I. Light-blue shaded regions highlight the redshift ranges of the Lyβ forest. The overlap between the gray bars and black bars yields Lyβ dark gaps as defined in this work.

Appendix A
Relationship between Lyβ Dark Gaps and Lyα Dark Gaps

To illustrate the effects of requiring Lyβ gaps to also be dark in the Lyα forest, here we explore the relationship between Lyβ dark gaps and Lyα dark gaps. In Figure A1 we overplot Lyβ-opaque regions (Flux$_{Ly\beta} < 0.02$ per 1 h^{-1} Mpc bin) on Lyα dark gaps as defined in Paper I. Although Lyβ-opaque regions overlap strongly with Lyα dark gaps, there do exist regions that are dark only in the Lyβ forest, e.g., the long Lyβ-opaque region toward CFHQS J1509−1749 that bridges two Lyα dark gaps, as shown in the figure. These cases are due to foreground Lyα absorption in the Lyβ forest. Requiring Lyβ gaps to also be dark in the Lyα forest partially avoids this kind of foreground contamination.

We further plot the length of Lyα dark gaps versus the length of corresponding Lyβ-opaque regions in Figure A2. Most of the long ($\geqslant$10 h^{-1} Mpc) Lyβ dark gaps appear in $L \geqslant 30$ h^{-1} Mpc Lyα dark gaps. Only 1 out of 23 long Lyβ-opaque regions contains transmission in Lyα and is split into two Lyβ dark gaps.

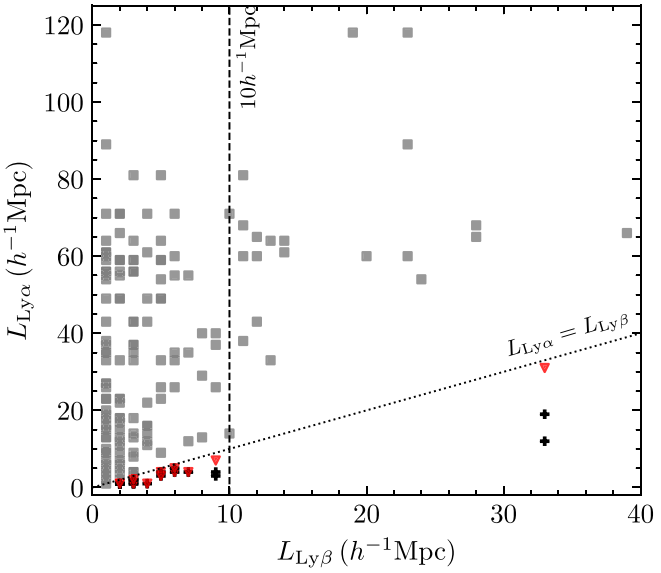

Figure A2. Length of Lyα dark gaps vs. length of Lyβ-opaque regions. For Lyβ dark gaps that are entirely within the redshift range of the Lyα dark gap, we plot the length of the Lyα gap vs. the length of the Lyβ gap with a gray square. Red triangles denote situations where not all 1 h^{-1} Mpc pixels in a Lyβ-opaque region have $\mathrm{Flux}_{Ly\alpha} < 0.05$ (Lyα dark gaps). The path lengths of Lyα dark gaps inside these Lyβ-opaque regions are marked with black crosses.

Appendix B
Metal-enriched Systems

In Figure B1 we display an overview of dark gaps with metal-enriched systems overplotted for the 27 QSO sight lines in our sample where the identification of metals is relatively complete and consistent. We label metal systems with redshifts in the Lyβ forest and in the foreground Lyα forest separately. These systems are included in a metal absorber catalog that will be presented in R. L. Davies et al. (2022, in preparation). Briefly, the `Python` application `Astrocook` was used to perform an automated search for Mg II, Fe II, C IV, Si IV, and N V absorbers and DLA-like systems probed by C II and other low-ionization species. Candidate absorbers were identified using a cross-correlation algorithm within `Astrocook` that searches for redshifts where significant absorption is present in all relevant transitions. Custom filtering algorithms and visual inspection were then used to remove false positives and produce the final absorber list.

We then investigate the correlation between long ($L \geqslant 10\ h^{-1}$ Mpc) dark gaps and metal systems. We find that the probability for a metal system in the Lyβ forest to lie in a long dark gap is $15\% \pm 9\%$, where the 68% confidence limit comes from bootstrapping these 27 sight lines 10,000 times. This probability is $31\% \pm 9\%$ in the case of a system in the corresponding foreground Lyα forest. In these calculations we count clustered metal absorbers with a separation of $<1\ h^{-1}$ Mpc as one system. By comparison, the probability that a randomly chosen point lies in a long dark gap is $22\% \pm 9\%$. Our results suggest that the correlation between long dark gaps and (foreground) metal systems is not highly significant, at least for this subsample. The relatively lower probability of finding metal absorbers within the redshifts of long dark gaps nevertheless potentially favors the association between high IGM Lyα opacities and galaxy underdensities (see also Becker et al. 2018; Kashino et al. 2020; Christenson et al. 2021).

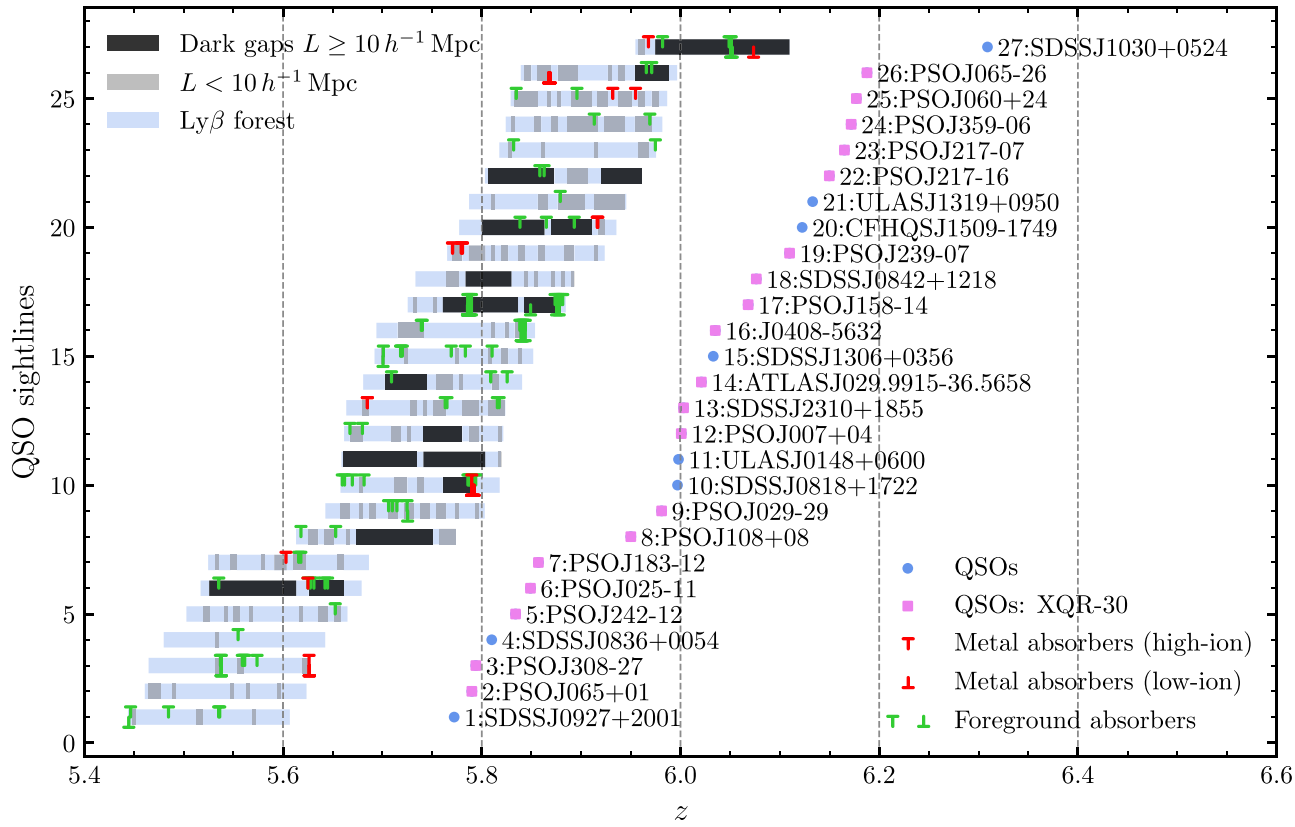

Figure B1. Similar to Figure 2, but with metal-enriched absorbers overplotted for 27 sight lines that have a relatively complete and consistent identification of metal-enriched absorbers (R. L. Davies et al. 2022, in preparation). We label high-ionization and low-ionization systems within the redshift of the Lyβ forest with red "$\top$" and "$\perp$" symbols, respectively. Foreground metal-enriched absorbers whose Lyα absorption would fall within the Lyβ forest are labeled with green symbols at the corresponding Lyβ redshifts.

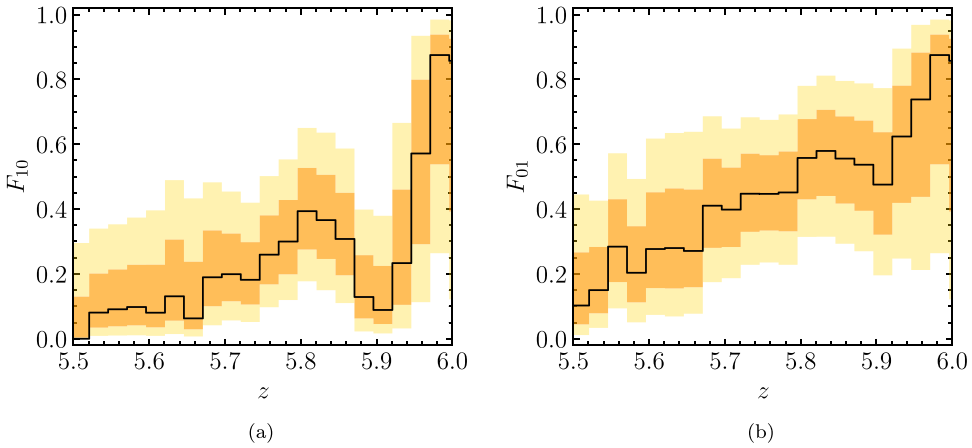

Figure C1. (a) Statistical uncertainty estimation for F_{10} shown in Figure 3(c). Dark- and light-shaded regions mark the 68% and 95% limits, respectively, of F_{10} based on Beta distribution. (b) Fraction of QSO spectra showing dark gaps with $L \geqslant 1\ h^{-1}$ Mpc.

Appendix C
Uncertainties in the Fraction of QSO Spectra Showing Dark Gaps

The evolution in F_{10} shown in Figure 4 shows a large drop near $z = 5.9$. To estimate the statistical fluctuations in F_{10}, we treat the "hit rate" of long dark gaps at individual redshifts as a binomial experiment defined by the number of hits (number of long dark gaps, $n_{\rm dark}$) inside a different number of trials (number of QSO sight lines, $n_{\rm qso}$). At a certain redshift, the posterior probability distribution function for the true "hit rate," x, can be expressed as a Beta distribution, $f(x;\ \alpha,\ \beta) \propto x^{\alpha-1}(1-x)^{\beta-1}$, with $\alpha = n_{\rm dark} + 0.5$ and $\beta = n_{\rm qso} - n_{\rm dark} + 0.5$, assuming a Jeffreys prior. As shown in Figure C1(a), the evolution of F_{10} is consistent with a monotonic increase with z within the 95% confidence intervals. We caution that the analysis here assumes that the "hit rates" at different redshifts are independent from each other.

While the dip could be due to statistical fluctuations, we nevertheless wish to check whether it may relate to possible biases in the data related to Lyβ absorption near that redshift. To check for possible systematic effects, we calculate the fraction of QSO spectra showing dark gaps of any length ($L \geqslant 1\ h^{-1}$ Mpc) as a function of redshift, F_{01}. As shown in Figure C1, the drop in F_{10} at $z \sim 5.9$ is not present in F_{01}. Instead, the evolution of Lyβ-opaque regions with redshift appears relatively smooth. We thus find no evidence of systematic effects in the data that would suggest lower absorption overall near $z = 5.9$.

Appendix D
Dark Gaps in a Lower-redshift Sample

Here we examine the extent to which strong, clustered absorbers associated with galaxies may be able to produce long dark gaps in the Lyβ forest. These (typically metal-enriched) absorbers may produce discrete absorption in either Lyβ over the redshift over the trough or Lyα at the corresponding foreground redshifts. They may also connect otherwise short dark gaps to form longer gaps. Of particular interest are very long gaps analogous to the $L = 28\ h^{-1}$ Mpc gap toward PSO J025−11. To test whether such gaps may be due to (circum)galactic absorbers rather than the IGM, we search for dark gaps at $z \lesssim 5.5$ in a sample of QSO lines of sight that lie at somewhat lower redshifts than our main sample. Because the IGM becomes increasingly transparent toward lower redshifts, any long dark gaps in this sample might signal a significant contribution from discrete systems associated with galaxies.

Our lower-redshift sample includes 27 ESI and X-Shooter spectra of QSOs over $5.0 < z_{\rm em} < 5.7$ from the Keck and VLT archives. The selection of targets is based on their redshift and is independent of foreknowledge of dark gaps. QSO spectra in this lower-redshift sample have S/N greater than 20 pixel^{-1} in the Lyβ forest. In order to account for the increased mean transmission at low redshifts, we conservatively use a higher flux threshold of 0.08 when searching for dark gaps. The ratio of mean flux in the Lyβ forest at $z = 4.8$ and 5.6 is about 3.2 (e.g., Fan et al. 2006; Eilers et al. 2019; Bosman et al. 2021); thus, a flux threshold of 4 times the high-redshift value is used.

Figure D1 shows dark gaps detected in this lower-redshift sample. No dark gaps longer than $10\ h^{-1}$ Mpc are detected. The lack of any long gaps in this sample suggests that extended gaps created largely by strong, discrete absorbers are rare, at least over $5 \lesssim z \lesssim 5.5$, which is reasonably close in redshift to our main sample. This increases our confidence that the $L = 28\ h^{-1}$ Mpc dark gap toward PSO J025−11 is likely to mainly arise from IGM absorption.

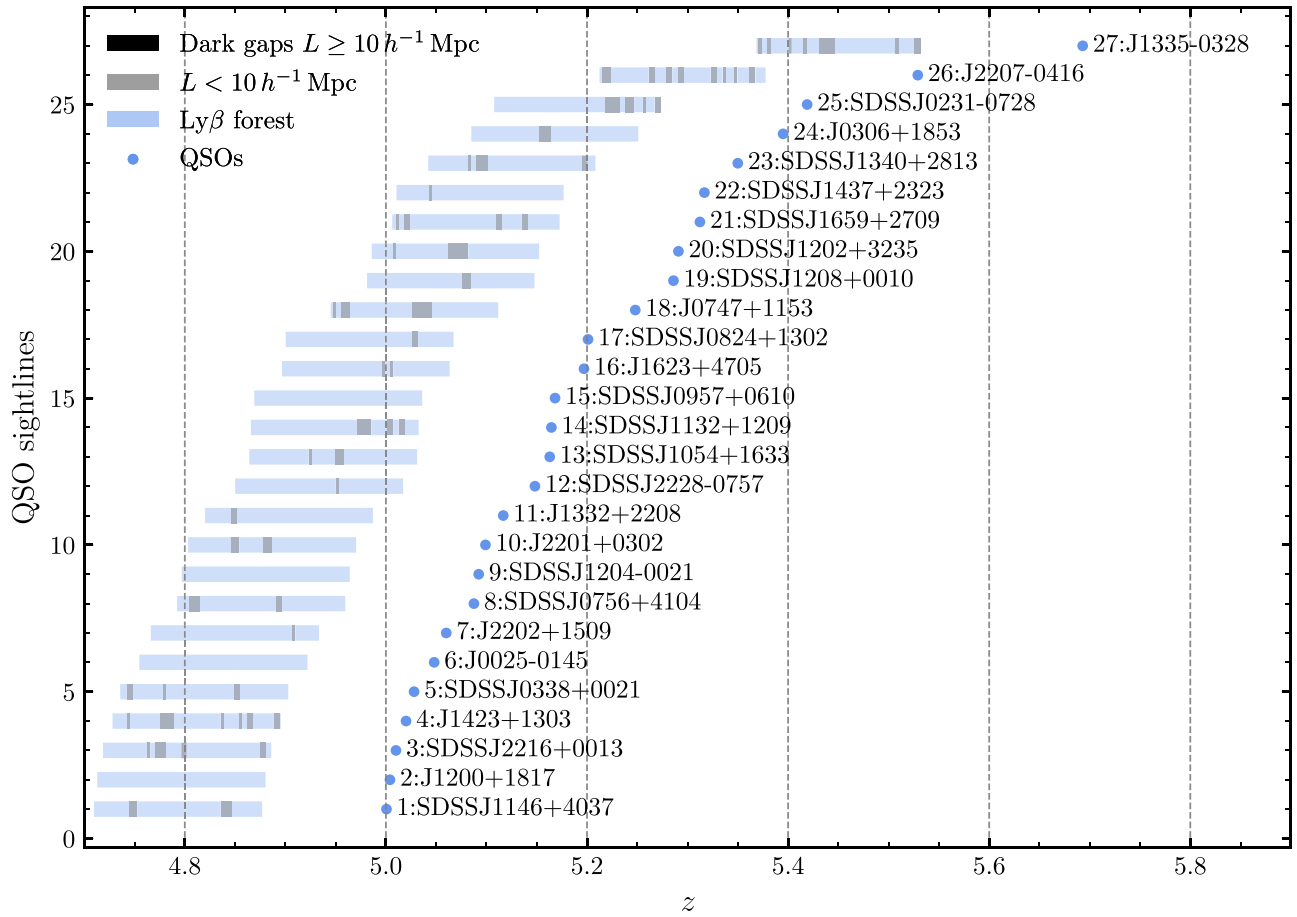

Figure D1. Similar to Figure 2, but showing dark gaps identified in the Lyβ forest from a lower-redshift sample.

ORCID iDs

Yongda Zhu https://orcid.org/0000-0003-3307-7525
George D. Becker https://orcid.org/0000-0003-2344-263X
Sarah E. I. Bosman https://orcid.org/0000-0001-8582-7012
Laura C. Keating https://orcid.org/0000-0001-5211-1958
Valentina D'Odorico https://orcid.org/0000-0003-3693-3091
Rebecca L. Davies https://orcid.org/0000-0002-3324-4824
Holly M. Christenson https://orcid.org/0000-0002-0421-065X
Eduardo Bañados https://orcid.org/0000-0002-2931-7824
Fuyan Bian https://orcid.org/0000-0002-1620-0897
Manuela Bischetti https://orcid.org/0000-0002-4314-021X
Huanqing Chen https://orcid.org/0000-0002-3211-9642
Frederick B. Davies https://orcid.org/0000-0003-0821-3644
Anna-Christina Eilers https://orcid.org/0000-0003-2895-6218
Xiaohui Fan https://orcid.org/0000-0003-3310-0131
Prakash Gaikwad https://orcid.org/0000-0002-2423-7905
Bradley Greig https://orcid.org/0000-0002-4085-2094
Martin G. Haehnelt https://orcid.org/0000-0001-8443-2393
Girish Kulkarni https://orcid.org/0000-0001-5829-4716
Samuel Lai https://orcid.org/0000-0001-9372-4611
Andrea Pallottini https://orcid.org/0000-0002-7129-5761
Yuxiang Qin https://orcid.org/0000-0002-4314-1810
Emma V. Ryan-Weber https://orcid.org/0000-0002-5360-8103
Fabian Walter https://orcid.org/0000-0003-4793-7880
Feige Wang https://orcid.org/0000-0002-7633-431X
Jinyi Yang https://orcid.org/0000-0001-5287-4242

References

Astropy Collaboration, Robitaille, T. P., Tollerud, E. J., et al. 2013, A&A, 558, A33
Bañados, E., Venemans, B. P., Mazzucchelli, C., et al. 2018, Natur, 553, 473
Becker, G. D., Bolton, J. S., Madau, P., et al. 2015, MNRAS, 447, 3402
Becker, G. D., D'Aloisio, A., Christenson, H. M., et al. 2021, MNRAS, 508, 1853
Becker, G. D., Davies, F. B., Furlanetto, S. R., et al. 2018, ApJ, 863, 92
Becker, G. D., Pettini, M., Rafelski, M., et al. 2019, ApJ, 883, 163
Boera, E., Becker, G. D., Bolton, J. S., & Nasir, F. 2019, ApJ, 872, 101
Bolton, J. S., Puchwein, E., Sijacki, D., et al. 2017, MNRAS, 464, 897
Bosman, S. E. I., Davies, F. B., Becker, G. D., et al. 2022, MNRAS, 514, 55
Bosman, S. E. I., Ďurovčíková, D., Davies, F. B., & Eilers, A. C. 2021, MNRAS, 503, 2077
Bosman, S. E. I., Fan, X., Jiang, L., et al. 2018, MNRAS, 479, 1055
Cain, C., D'Aloisio, A., Gangolli, N., & Becker, G. D. 2021, ApJL, 917, L37
Carnall, A. C. 2017, arXiv:1705.05165
Choudhury, T. R., Paranjape, A., & Bosman, S. E. I. 2021, MNRAS, 501, 5782
Christenson, H. M., Becker, G. D., Furlanetto, S. R., et al. 2021, ApJ, 923, 87
Cupani, G., D'Odorico, V., Cristiani, S., et al. 2020, Proc. SPIE, 11452, 114521U
Davies, F. B., Becker, G. D., & Furlanetto, S. R. 2018a, ApJ, 860, 155
Davies, F. B., Bosman, S. E. I., Furlanetto, S. R., Becker, G. D., & D'Aloisio, A. 2021, ApJL, 918, L35
Davies, F. B., Hennawi, J. F., Bañados, E., et al. 2018b, ApJ, 864, 142
Davies, F. B., Hennawi, J. F., Bañados, E., et al. 2018c, ApJ, 864, 143
de Belsunce, R., Gratton, S., Coulton, W., & Efstathiou, G. 2021, MNRAS, 507, 1072
Eilers, A.-C., Davies, F. B., Hennawi, J. F., et al. 2017, ApJ, 840, 24
Eilers, A.-C., Davies, F. B., & Hennawi, J. F. 2018, ApJ, 864, 53

Eilers, A.-C., Hennawi, J. F., Davies, F. B., & Oñorbe, J. 2019, ApJ, 881, 23
Eilers, A.-C., Hennawi, J. F., Decarli, R., et al. 2020, ApJ, 900, 37
Fan, X., Strauss, M. A., Becker, R. H., et al. 2006, AJ, 132, 117
Furlanetto, S. R., Hernquist, L., & Zaldarriaga, M. 2004, MNRAS, 354, 695
Gaikwad, P., Rauch, M., Haehnelt, M. G., et al. 2020, MNRAS, 494, 5091
Gaikwad, P., Srianand, R., Haehnelt, M. G., & Choudhury, T. R. 2021, MNRAS, 506, 4389
Gallerani, S., Ferrara, A., Fan, X., & Choudhury, T. R. 2008, MNRAS, 386, 359
Gnedin, N. Y., Becker, G. D., & Fan, X. 2017, ApJ, 841, 26
Greig, B., Mesinger, A., Davies, F. B., et al. 2022, MNRAS, 512, 5390
Haardt, F., & Madau, P. 2012, ApJ, 746, 125
Hoag, A., Bradač, M., Huang, K., et al. 2019, ApJ, 878, 12
Hu, W., Wang, J., Zheng, Z.-Y., et al. 2019, ApJ, 886, 90
Hunter, J. D. 2007, CSE, 9, 90
Jung, I., Finkelstein, S. L., Dickinson, M., et al. 2020, ApJ, 904, 144
Kashino, D., Lilly, S. J., Shibuya, T., Ouchi, M., & Kashikawa, N. 2020, ApJ, 888, 6
Keating, L. C., Kulkarni, G., Haehnelt, M. G., Chardin, J., & Aubert, D. 2020a, MNRAS, 497, 906
Keating, L. C., Weinberger, L. H., Kulkarni, G., et al. 2020b, MNRAS, 491, 1736
Kulkarni, G., Keating, L. C., Haehnelt, M. G., et al. 2019, MNRAS, 485, L24
Mann, H. B., & Whitney, D. R. 1947, Ann. Math. Stat., 18, 50
Mason, C. A., Fontana, A., Treu, T., et al. 2019, MNRAS, 485, 3947
Mason, C. A., Treu, T., Dijkstra, M., et al. 2018, ApJ, 856, 2
McGreer, I. D., Mesinger, A., & D'Odorico, V. 2015, MNRAS, 447, 499
McGreer, I. D., Mesinger, A., & Fan, X. 2011, MNRAS, 415, 3237
Muñoz, J. B., Qin, Y., Mesinger, A., et al. 2022, MNRAS, 511, 3657
Nasir, F., & D'Aloisio, A. 2020, MNRAS, 494, 3080
Paschos, P., & Norman, M. L. 2005, ApJ, 631, 59
Planck Collaboration, Ade, P. A. R., Aghanim, N., et al. 2014, A&A, 571, A16
Planck Collaboration, Aghanim, N., Akrami, Y., et al. 2020, A&A, 641, A6
Puchwein, E., Haardt, F., Haehnelt, M. G., & Madau, P. 2019, MNRAS, 485, 47
Qin, Y., Mesinger, A., Bosman, S. E. I., & Viel, M. 2021, MNRAS, 506, 2390
Sheinis, A. I., Bolte, M., Epps, H. W., et al. 2002, PASP, 114, 851
Songaila, A., & Cowie, L. L. 2002, AJ, 123, 2183
van der Walt, S., Colbert, S. C., & Varoquaux, G. 2011, CSE, 13, 22
Vernet, J., Dekker, H., D'Odorico, S., et al. 2011, A&A, 536, A105
Villasenor, B., Robertson, B., Madau, P., & Schneider, E. 2021, arXiv:2111.00019
Wang, F., Davies, F. B., Yang, J., et al. 2020, ApJ, 896, 23
Weinberger, L. H., Haehnelt, M. G., & Kulkarni, G. 2019, MNRAS, 485, 1350
Wold, I. G. B., Malhotra, S., Rhoads, J., et al. 2022, ApJ, 927, 36
Yang, J., Wang, F., Fan, X., et al. 2020a, ApJ, 904, 26
Yang, J., Wang, F., Fan, X., et al. 2020b, ApJL, 897, L14
Zhu, Y., Becker, G. D., Bosman, S. E. I., et al. 2021, ApJ, 923, 223